CORE
Metadata, citation and similar papers at core.ac.uk
Provided by CERN Document Server

Mon. Not. R. Astron. Soc. **000**, 000–000 (0000) Printed 14 March 2007 (MN LATEX style file v2.2)

Adaptive Contouring – an efficient way to calculate microlensing light curves of extended sources

M. Dominik⋆†
SUPA, University of St Andrews, School of Physics & Astronomy, North Haugh, St Andrews, KY16 9SS, United Kingdom

arXiv:astro-ph/0703305v1 13 Mar 2007

14 March 2007

ABSTRACT

The availability of a robust and efficient routine for calculating light curves of a finite source magnified due to bending its light by the gravitational field of an intervening binary lens is essential for determining the characteristics of planets in such microlensing events, as well as for modelling stellar lens binaries and resolving the brightness profile of the source star. However, the presence of extended caustics and the fact that the images of the source star cannot be determined analytically while their number depends on the source position (relative to the lens system), makes such a task difficult in general. Combining the advantages of several earlier approaches, an adaptive contouring algorithm is presented, which only relies on a small number of simple rules and operations on the adaptive search grid. By using the parametric representation of critical curves and caustics found by Erdl & Schneider (1993), seed solutions to the adaptive grid are found, which ensures that no images or holes are missed.

Key words: gravitational lensing – methods: numerical – planetary systems – binaries: general – stars: atmospheres.

1 INTRODUCTION

In order to determine the characteristics of planets that reveal their existence in microlensing events, to model stellar lens binaries, and to distinguish between these configurations, efficient algorithms for calculating light curves of extended source stars due to microlensing of a binary lens system are required. For a single point-like lens, the magnification of a point source is an analytic function (Einstein 1936), the magnification of a uniformly bright circular source can be expressed by means of elliptic integrals (Witt & Mao 1994), and is therefore a one-dimensional integral over a semi-analytic function in general, which can be approximated by the product of the point-source magnification with a characteristic function of a single variable, depending on the source brightness profile (Gould 1994). For a binary lens, however, the complexity increases enormously. Whereas a point source affected by a single point-mass lens always has two images, with the only exception of lens and source being perfectly aligned, binary lenses yield either three or five images depending on the source position relative to the lens, where three-image and five-image regions are separated by extended caustics. This implies that one cannot as easily integrate over the source position as in the single-lens case. Moreover, the point-source magnification cannot be expressed as analytic or semi-analytic function, but needs to be determined by means of solving a fifth-order complex polynomial (Witt & Mao 1995). While a two-dimensional integration over the source is possible in principle, one carefully needs to keep track of the caustic and needs to deal with a divergent integrand as it is approached. While ray-shooting algorithms (Kayser et al. 1986; Schneider & Weiß 1987) overcome the need for determining the images by creating a magnification map based on mapping the image plane to the corresponding true source positions, summing the hits within a source still is a discretization of a two-dimensional integration. On the other hand, Schramm & Kayser (1987) have found that contour plot routines offer a simple way for plotting the images of an extended source, which avoids the inversion of the lens equation. Dominik (1995) later showed that in addition to providing plots, the same technique can be used to efficiently derive numerical values, and in particular to determine the magnification of extended sources as well as of the incurred astrometric shift in the centroid of their unresolved imges by applying Green's theorem (Dominik 1998). In fact, determining the image area from a contour plot is similar to the ray-shooting magnification map approach in mapping an image plane grid to the respective source position, but rather than the magnification being determined over the source area, an integral in the image plane is discretized.

In this paper, an algorithm is presented that determines the magnification from the image contour using an adaptive grid rather than a static one. By recognizing the positions of the images of the source centre, which can be calculated by solving a fifth-order complex polynomial (Witt & Mao 1995), the fact that holes in the images must include the positions of the point-like deflectors, and by finding all images stretching over critical curves using a parametric representation based on the classification of the topology of

⋆ Royal Society University Research Fellow
† E-mail: md35@st-andrews.ac.uk

the critical curves and caustics by Erdl & Schneider (1993), it is ensured that all images for a binary lens are appropriately considered.

While Sect. 2 reviews the basic properties of gravitational lensing, Sect. 3 presents the adaptive contouring algorithm and Sect. 4 shows how to determine the magnification of an extended source star from the image contour line. Sect. 5 discusses the critical curves and caustics of a binary point-mass lens in order to derive an algorithm for finding a point inside an image stretching over a critical curve. Example light curves are shown in Sect. 6 before the paper concludes with a short summary in Sect. 7.

2 GRAVITATIONAL LENSING

Light received from a source object at distance $D_{\rm S}$ is bent due to the gravitational field of a thin sheet of matter at a distance $D_{\rm L}$ with surface mass density $\Sigma(\boldsymbol{\xi}')$ by the angle (Schneider 1985)

$$\hat{\boldsymbol{\alpha}}(\boldsymbol{\xi}) = \frac{4G}{c^2} \int \Sigma(\boldsymbol{\xi}') \, \frac{\boldsymbol{\xi}-\boldsymbol{\xi}'}{|\boldsymbol{\xi}-\boldsymbol{\xi}'|^2} \, {\rm d}^2\boldsymbol{\xi}' \,. \tag{1}$$

For $\boldsymbol{\beta}$ denoting the true source position angle and $\boldsymbol{\theta}$ the apparent position angle of its observed images, this implies the *lens equation*

$$\boldsymbol{y}(\boldsymbol{x}) = \boldsymbol{x} - \boldsymbol{\alpha}(\boldsymbol{x}) \,, \tag{2}$$

where $\boldsymbol{x} = \boldsymbol{\theta}/\theta_0$, $\boldsymbol{y} = (D_{\rm L}/D_{\rm S})\,(\boldsymbol{\beta}/\theta_0)$, and

$$\boldsymbol{\alpha}(\boldsymbol{x}) = \frac{4G}{c^2} \, \frac{D_{\rm S}-D_{\rm L}}{D_{\rm L} D_{\rm S}} \, \frac{1}{\theta_0^2} \int \kappa(\boldsymbol{x}') \, \frac{\boldsymbol{x}-\boldsymbol{x}'}{|\boldsymbol{x}-\boldsymbol{x}'|^2} \, {\rm d}^2\boldsymbol{x}' \tag{3}$$

with $\kappa(\boldsymbol{x}') = (D_{\rm L}\theta_0)^2 \, \Sigma(D_{\rm L}\theta_0\boldsymbol{x}')$. It provides a surjective mapping of the image position $\boldsymbol{x}$ to the source position $\boldsymbol{y}$, but the lack of injectivity means that a source may have more than just one image.

At *critical points* $\boldsymbol{x}_{\rm c}$, defined by

$$\det\left(\frac{\partial \boldsymbol{y}}{\partial \boldsymbol{x}}\right)(\boldsymbol{x}_{\rm c}) = 0 \,, \tag{4}$$

two images merge, so that the number of images changes if and only if the source passes a *caustic point* $\boldsymbol{y}_{\rm c} = \boldsymbol{y}(\boldsymbol{x}_{\rm c})$. In general, critical points and caustic points form closed curves, known as *critical curves* and *caustics* unless these degenerate into a point in special cases. The conservation of surface brightness by gravitational lensing, i.e. $I(\boldsymbol{x}) = I[\boldsymbol{y}(\boldsymbol{x})]$, implies that the total magnification of a point source is given by

$$A(\boldsymbol{y}) = \sum_{\{\boldsymbol{x}^{(i)}\,|\,\boldsymbol{y}=\boldsymbol{y}(\boldsymbol{x}^{(i)})\}} \left[\det\left(\frac{\partial \boldsymbol{y}}{\partial \boldsymbol{x}}\right)\left(\boldsymbol{x}^{(i)}\right)\right]^{-1} \tag{5}$$

so that it diverges if the source comes to lie on a caustic.

For an extended source, as a consequence of Liouville's theorem, source and lens contours of same brightness correspond. This means that if a source contour is described by an implicit function $F(\boldsymbol{y};\boldsymbol{p}) = 0$, with $\boldsymbol{p}$ being a parameter vector specifying the contour, then all its image contours are given by $F[\boldsymbol{y}(\boldsymbol{x});\boldsymbol{p}] = 0$. Therefore, a contour plot provides image contour lines without inversion of the lens equation (Schramm & Kayser 1987).

3 ADAPTIVE CONTOURING

3.1 Data structure and algorithm

A search grid in the image plane needs to be large enough to cover all images and dense enough, so that no images or holes in the images are missed. While fulfilling these two condition, the grid resolution should be kept as low as possible. Obviously, an adaptive grid that just provides higher resolution in regions where this is required turns out to be superior to a fixed-resolution grid.

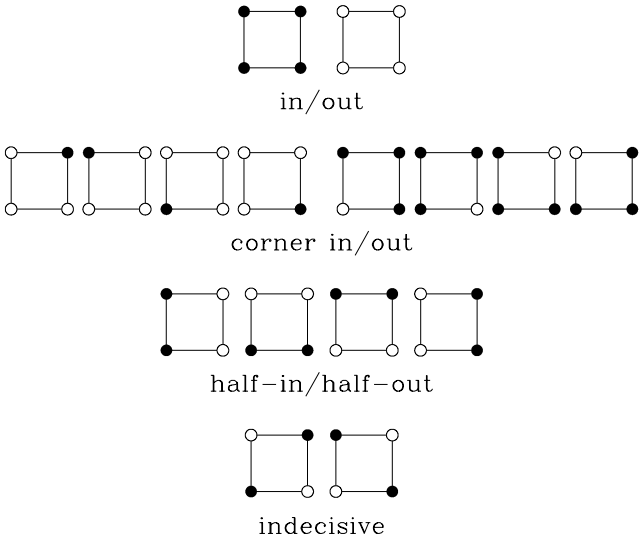

Figure 1. The 16 different elementary squares, defined by whether each of the corners is inside or outside the contour line, where 'inside' is marked by a filled black circle and 'outside' is marked by an open circle (filled white). While in- or out-squares are considered fully inside or outside the contour line and therefore of no further interest, the contour line passes through squares of type 'corner in/out' or 'half-in/half-out'. All four edges of squares with corners alternating between inside and outside along their boundary are cut by the contour line, while it is not clear which edges the contour line runs between, making such squares indecisive.

Such an adaptive grid can be built by hierachically nesting squares that represent parts of the image plane. In order to approximate the position of the contour line, a ray is shot to the corresponding image position given by the defined mapping, Eq. (2), and it is noted whether the corresponding true source position falls inside or outside the source contour. In this respect, the proposed algorithm resembles the ray-shooting approach (Kayser et al. 1986; Schneider & Weiß 1987), but the indicator of whether the light ray hits the source is kept with the image position. In fact, with the conservation of surface brightness, as pointed out in Sect. 2, the image position has the same relation (inside or outside) with respect to the image contour as the corresponding source position to the source contour.

A square with the inside/outside indicators for its corners constitutes the elementary data structure, out of which all relevant information about the image plane is constructed. Being characterized by its four indicators, there are $2^4 = 16$ types of elementary squares, shown in Fig. 1. 12 of these elementary squares, namely those of type 'corner in/out' or 'half-in/half-out', define part of the contour line, which crosses two edges of the square whose corners have different status. If two opposite corners are found to be inside and the other two corners outside, the contour needs to cross all four edges, but it is not clear which edges it connects. Therefore, such indecisive squares need to be subdivided in order to improve the resolution (this is rule 1 below).

The length of an edge of a square of depth k is $2^{-k}a$, where a denotes a unit size. Squares are nested so that each square S^k_{mn} of depth k either contains 4 subsquares of depth $k+1$ each sharing a different corner with S^k_{mn}, or S^k_{mn} does not have any subsquare.

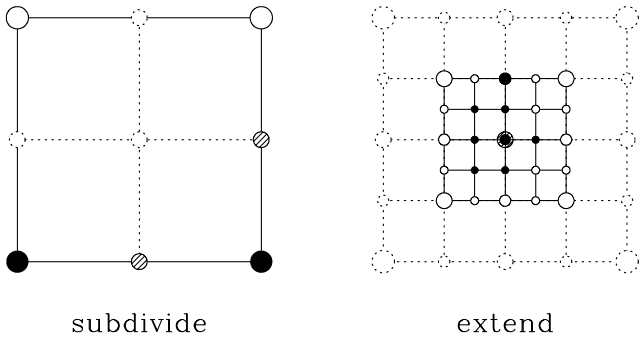

Figure 2. The two operations `subdivide` and `extend`. The elements that are being added are shown with dotted lines or shaded areas. The size of the inside/outside indicators reflects the depth of the respective square.

The minimal and initial data structure consists of a square of depth -1 with 4 subsquares of depth 0.

The version of the adaptive contouring algorithm presented here uses just two operations on the data structure, `subdivide` and `extend`, illustrated in Fig. 2. While `subdivide` creates 4 sub-squares of depth $k+1$ to a specified square of depth k, `extend` enlarges the range covered by the adaptive search grid by creating a new top-level grid with the same centre as the previous one but twice the length of an edge. The following conditions require invocation of the operations `extend` (condition $\mathcal{E}$) or `subdivide` (conditions $\mathcal{S}_1$ to $\mathcal{S}_3$):

- *Condition* $\mathcal{E}$: A point at the boundary of the outermost square is found to be inside
- *Condition* $\mathcal{S}_1$: Square is indecisive, i.e. it has alternating inside/outside corners along its boundary
- *Condition* $\mathcal{S}_2$: Adjoining corners of a square have same status, but status changes among evaluated points (corners of subsquares) along the connecting edge
- *Condition* $\mathcal{S}_3$: Square of depth smaller than a specified $k_{\min}$ is of type 'corner in/out' or 'half-in/half-out'

The operations following conditions $\mathcal{E}$, $\mathcal{S}_1$ and $\mathcal{S}_2$ eliminate all problematic cases and need to be executed for squares of all depths before the contour line can be determined, whereas calling `subdivide` on all squares fulfilling condition $\mathcal{S}_3$ leads to all squares that contain the contour line having a depth of at least $k_{\min}$. Application of `extend` can cause condition $\mathcal{E}$ only to arise in the new surrounding square. Similarly, the application of `subdivide` can cause condition $\mathcal{S}_1$ only to arise in subsquares. In contrast, adjoining squares need to be checked for condition $\mathcal{S}_2$, while any of the conditions may arise in new subsquares created on the application of `extend`. For this reason, `extend` or `subdivide` are executed recursively if conditions $\mathcal{E}$ or $\mathcal{S}_1$ arise, whereas if modifications lead to squares fulfilling conditions $\mathcal{S}_2$ or $\mathcal{S}_3$, these are put on stacks specific to the condition and the depth of the respective square. Since squares for any depth need to be checked for condition $\mathcal{S}_2$, a square fulfilling it needs to be placed on the stack even if it has already been placed on a stack related to condition $\mathcal{S}_3$. This can leave squares on stacks for condition $\mathcal{S}_3$ that have already been subdivided. If such squares are encountered, they must be ignored and removed from the stack.

In order to find the contour line for a depth $k_{\min}$, from the top level to the depth $k_{\min}-1$, squares are taken from the corresponding stack related to condition $\mathcal{S}_3$ and the operation `subdivide` is executed. This might cause conditions $\mathcal{E}$ and $\mathcal{S}_1$ to arise and corresponding `extend` or `subdivide` operations being carried out, while squares fulfilling conditions $\mathcal{S}_2$ are placed on a respective stack. Subsequently, all stacks with squares fulfilling $\mathcal{S}_3$ are being cleared by pulling the respective squares from them and executing the `subdivide` operation. If the application of `extend` for squares fulfilling condition $\mathcal{E}$ or of `subdivide` for squares fulfilling condition $\mathcal{S}_2$ or were carried out, this might have created squares fulfilling condition $\mathcal{S}_3$, so that the full procedure needs to be repeated until this is not the case. After all these operations have been applied, the stacks with squares fulfilling condition $\mathcal{S}_3$ with depth $k \geqslant k_{\min}$ hold the squares from which to determine the contour line. Fig. 3 illustrates the representation of the image plane by the nested squares that results from applying the adaptive contouring algorithm for a given resolution depth $k_{\min}$.

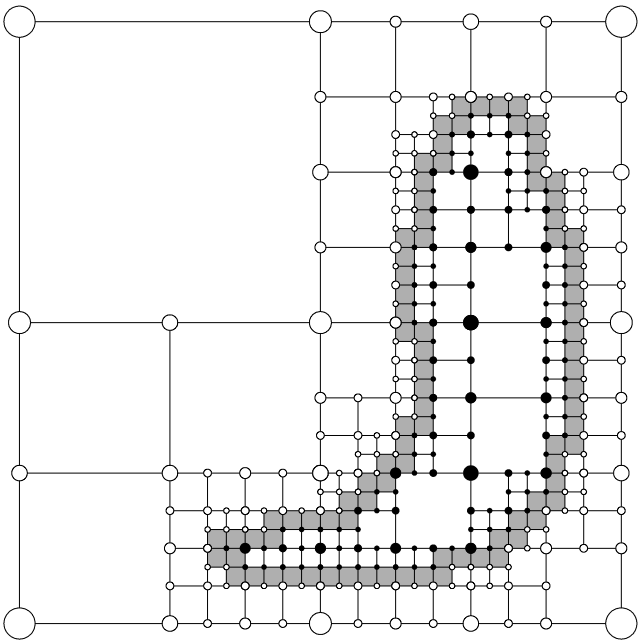

Figure 3. Representation of contour at a given resolution depth by set of nested squares after the rules of the adaptive contouring algorithm have been applied. Filled black circles mark corners that are inside the contour, while open (filled white) circles mark those outside the contour. Their size reflects the depth of the outermost square this corner belongs to. The squares of types 'corner in/out' or 'half-in/half-out' (see Fig. 1) contain the contour line and are shaded in grey.

As pointed out in detail in Sect. 4, The desired magnification of the source star can be obtained from an evaluation of approximated contour lines for a series of increasing $k_{\min}$ until a desired accuracy is reached. Rather than subdiving all squares that constitute the contour line to a certain given depth, it would be advantageous to pick those squares that are expected to provide the largest gain in improving the estimate of the source magnification. However, this would require some advanced bookkeeping.

3.2 Finding all images and holes

The essential need to find all segments of the contour line can be met by inserting a representation of at least one point inside each image and each hole. A point that falls exactly onto a corner is represented directly in the data structure. Otherwise, one can use the fact that with any point that is not exactly on the contour line, there is always a region around it that is either inside or outside.

A point can then be represented by the surrounding region which can take the form of a single in- or out-square if the point is inside a square and by two adjoining in- or out-squares if the point falls on their common edge. If 1) for each region enclosed by a contour line, at least one point is represented by an inside corner or one or two in-squares, 2) at least one point inside each hole (i.e. a region surrounded by a contour line that is not enclosed) is represented by an outside corner or one or two out-squares and 3) the representing squares do not overlap, the adaptive contouring algorithm is guaranteed to find all segments of the contour line, so that no enclosed region or hole is missed.

The condition for the representing squares not to overlap can be met by determining a maximal size for the square surrounding each point to be inserted. A simple choice is to consider touching squares of the same size around this point and each of the other points, use the minimal size and round it to the next smaller $2^{-k_i}a$. If the point to be inserted into the data structure does not fall into the top-level square, one needs to call `extend` until this requirement is met. Subsequently, starting at the top-level square, while the depth is smaller than the minimal depth k_i or not all corners have the right status (inside for images, outside for holes), one needs to branch into the larger-depth subsquare that contains the point. If no subsquares exist, these must be created by a `subdivide` operation. If the point to be inserted falls onto an existing corner, one can stop, whereas if the point falls onto an edge, the search needs to be split into searches inside a square right and left (for a horizontal edge) or above and below (for a vertical edge). Such a split becomes necessary at most once.

3.3 Image contours for binary point-mass lenses

Let us consider the special case of a lens of total mass M, composed of two point lenses with mass fractions m_1 and $m_2 = 1-m_1$ that are separated by the angle $d\,\theta_{\rm E}$, where

$$\theta_{\rm E} = \sqrt{\frac{4GM}{c^2}\,\frac{D_{\rm S}-D_{\rm L}}{D_{\rm L}D_{\rm S}}}\,. \tag{6}$$

With the choice $\theta_0 = \theta_{\rm E}$, the lens equation, Eq. (2), then reads

$$\begin{aligned}\boldsymbol{y}(\boldsymbol{x}) \;&=\; \boldsymbol{x} - m_1\frac{\boldsymbol{x}+(1-m_1)(d,0)}{|\boldsymbol{x}+(1-m_1)(d,0)|^2} \;- \\ &\quad -\,(1-m_1)\frac{\boldsymbol{x}-m_1(d,0)}{|\boldsymbol{x}-m_1(d,0)|^2}\,,\end{aligned} \tag{7}$$

where the origin of the coordinate system coincides with the centre of mass of the binary-lens system and the line connecting the two components is along the y_1-axis. Such a binary point-mass lens is not only a fair model for a stellar binary but also for an isolated star orbited by planets, where usually the effect of just a single planet dominates.

If an extended source is completely outside the caustics, its image contours surround three images, whereas these surround five images if the extended source is completely inside. Every point inside the source has a point image inside one of the images of the extended source, so that the images of any point inside the source, in particular the source centre, provide a seed for finding the image contour lines as pointed out in the previous subsection. These can be found straightforwardly by solving a fifth-order complex polynomial (Witt & Mao 1995). If part of the source is inside and part of it outside, the number of images differs among its enclosed points, so that between one and four images of the extended source can occur, where some contour lines cross critical curves, so that the enclosed images of the source contain more than a single image of points within the source that are inside the caustic. Finding a point inside the caustic and determining its images would provide all five necessary seeds. While this is not trivial, one can take a slightly different approach. As long as the source encloses a cusp, the contour line encloses at least one image of any point inside the caustic, so that the at least three images of the source centre are sufficient as seeds. The only remaining case is that the source extends over a single fold caustic, so that one of its images stretches over a critical curve with no position inside mapping to the source centre. A point inside such an image can be found as a point on the critical curve that maps to a local minimum of the distance between source centre and caustic. Finding such a point inside requires some sophisticated analysis of the critical curves and caustics of the underlying binary lens. This is pointed out in detail in Sect. 5. Seeds for holes are found easily for a binary point-mass lens since these need to include one of the positions of the two point-mass constituents. With the lens equation, Eq. (7), having poles there, it is sensible to ensure that these positions are defined to be outside any closed contour.

Fig. 4 shows the data structure after the seed points have been inserted for an example configuration, for which $m_1 = 0.3$, $d = 1.2$ and the centre of a circular source of angular radius $\rho_\star\,\theta_{\rm E}$, where $\rho_\star = 0.2$, is located at $\boldsymbol{y} = (-0.1, 0.45)$ along with the image contour lines, the critical curve, and the source contour with the caustic. Around the positions of the two point masses, namely $(-0.84, 0)$ and $(0.36, 0)$, marked by crosses, two out-squares representing holes have been inserted (these positions falling onto an edge), whereas the three images of the source centre have been surrounded by in-squares. However, there is a fourth image stretching over a critical curve, where a seed has been given by a local minimum of the distance between the source centre and the caustic, as described in detail in Sect. 5.4.

4 IMAGE AREA AND MAGNIFICATION

The conservation of surface brightness by gravitational lensing implies that for uniformly bright sources, the magnification equals the ratio between the total area of the images and that of the unaffected source. This means that the problem of calculating the magnification of a uniformly bright source reduces to that of determining the area of its images.

As exploited by Dominik (1995, 1998), Green's theorem allows to transform an integral over a region R into an integral over its boundary ∂R. Namely, for two functions $P(x_1, x_2)$ and $Q(x_1, x_2)$ that are continous in R and whose partial derivatives $\partial P/\partial x_2$ and $\partial Q/\partial x_1$ are also continuous in R,

$$\int\limits_R \left(\frac{\partial Q}{\partial x_1} - \frac{\partial P}{\partial x_2}\right)\,{\rm d}x_1\,{\rm d}x_2 = \int\limits_{\partial R} P\,{\rm d}x_1 + Q\,{\rm d}x_2\,. \tag{8}$$

In particular, for the area of R, one has $\partial Q/\partial x_1 - \partial P/\partial x_2 = 1$, which is fulfilled with the choice $P(x_1, x_2) = -\frac{1}{2}x_2$ and $Q(x_1, x_2) = \frac{1}{2}x_1$, so that the magnification of a uniformly bright circular source star with angular radius $\rho_\star\,\theta_{\rm E}$ reads

$$A(\boldsymbol{y}^{(0)}, \rho_\star) = \frac{1}{2\pi\,\rho_\star^2}\int\limits_{\partial R} x_1\,{\rm d}x_2 - x_2\,{\rm d}x_1\,, \tag{9}$$

where ∂R denotes the union of the contours of all its images.

An approximation of the contour line can be obtained from an inspection of all squares of types 'corner in/out' or 'half-in/half-out'. The intermediate value theorem implies that the continuous

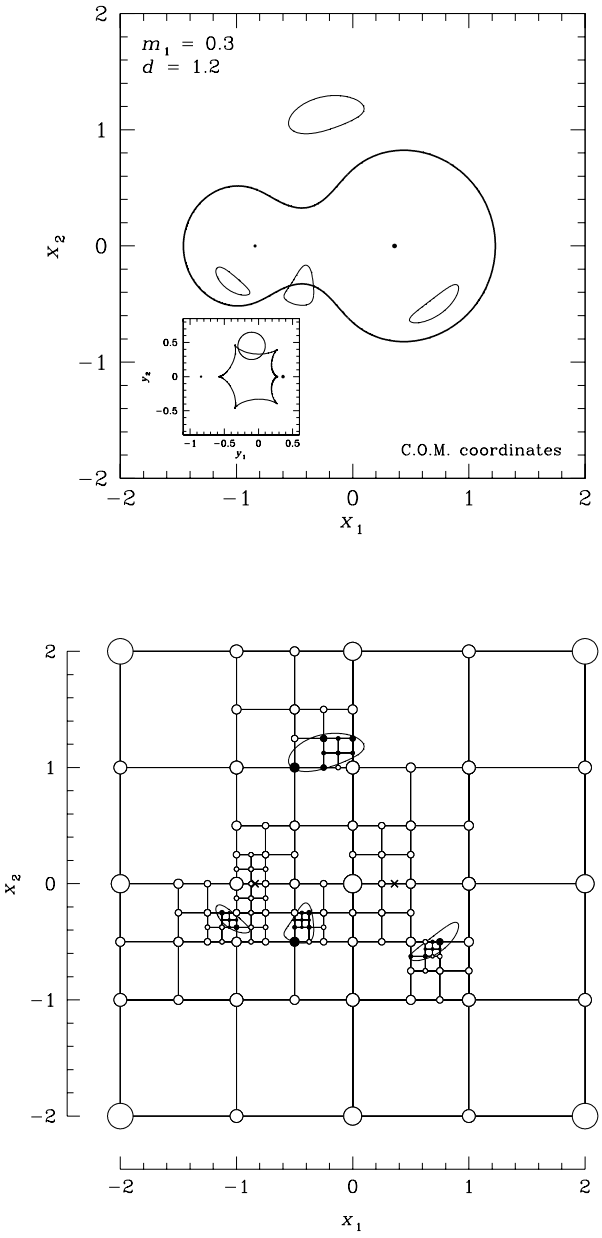

Figure 4. (top) Image contours for a circular source star resulting from the deflection of light by the gravitational field of a binary lens for an example configuration. The coordinates denote angles on the sky in multiples of the angular Einstein radius $\theta_{\rm E}$, defined by Eq. (6), where the coordinate origin coincides with the centre of mass of the binary-lens system. The separation of the two point masses with fractional mass $m_1 = 0.3$ (left) and $1 - m_1 = 0.7$ (right) in units of the angular Einstein radius $\theta_{\rm E}$ has been chosen as $d = 1.2$. The thick line shows the critical curve. The inset shows the caustic along with the source contour, where the source centre is located at $\boldsymbol{y} = (-0.1, 0.45)$ and its angular radius in units of $\theta_{\rm E}$ is $\rho_\star = 0.2$. (bottom) Set of nested squares with inside/outside indicators constituting the data structure that represents the image plane after seeds for the image and the hole positions have been inserted. Image seeds were the three images of the source centre and a point on the critical curve that maps to a local minimum of the distance between source centre and caustic. Hole seeds were the positions of the two point masses, namely $(-0.84, 0)$ and $(0.36, 0)$, marked as crosses. In lightface, the image contour lines are indicated. The size of the inside/outside indicators (black for inside, white for outside) reflect the depth of the respective outermost square.

function $F[\boldsymbol{y}(\boldsymbol{x}), \boldsymbol{p}]$ restricted to the edge of a square has at least one root if the signs at the corners differ, which means that the contour line has to cross the edge. For elementary square of types 'corner in/out' or 'half-in/half-out', see Fig. 1, there are two such edges whose crossings with the image contour line define its entry to and exit from the respective square. Usually contour plot algorithms determine the cut of the contour line with the edge by linear interpolation using the values of $F[\boldsymbol{y}(\boldsymbol{x}), \boldsymbol{p}]$ at the corners. However, since the images are dominated by convex contours, this choice systematically leads to an underestimation of the enclosed area. From practice, it has emerged that simply using the midpoint between the corners provides an estimate that on average deviates less from the true image area for moderate precisions. It might happen that the image contour line runs through squares of different depth. For adjacent squares of different depth joining at an edge, the contour line has to be put through the edge of the square with larger depth, i.e. the smaller one.

Let us consider a circular source with angular radius $\rho_\star\,\theta_{\rm E}$ whose center is at $\boldsymbol{y}^{(0)}$, so that $\boldsymbol{p} = (\boldsymbol{y}^{(0)}, \rho_\star)$ constitutes the respective parameter vector. For the square denoted by the running index i, let $(x_1^{(i)}, x_2^{(i)})$ and $(x_1^{(i+1)}, x_2^{(i+1)})$ be the adopted intersections of the edges with the contour line. A symmetric discretization of Eq. (9) then yields

$$\begin{aligned} A(\boldsymbol{y}^{(0)}, \rho_\star) &= \frac{1}{4\pi\rho_\star^2} \sum_{i=1}^{n} \Big[(x_1^{(i)} + x_1^{(i+1)})\,(x_2^{(i+1)} - x_2^{(i)}) - \\ &\quad - (x_2^{(i)} + x_2^{(i+1)})\,(x_1^{(i+1)} - x_1^{(i)}) \Big] \\ &= \frac{1}{4\pi\rho_\star^2} \sum_{i=1}^{n} \left(x_1^{(i)} x_2^{(i+1)} - x_2^{(i)} x_1^{(i+1)} \right) . \end{aligned} \quad (10)$$

The absolute error in the area cannot exceed the sum of the area of all squares through which the contour line runs, but it can be expected to be much smaller than that. While the ratio ε between these squares and the approximated enclosed area gives some measure for the quality of the approximation, it vastly overestimates the typical error. However, a suitable value for ε can be chosen from testing how its variation affects the final result.

For a general surface brightness $I[\boldsymbol{y}(\boldsymbol{x}); \boldsymbol{y}^{(0)}, \rho_\star]$, one finds

$$\begin{aligned} A(\boldsymbol{y}^{(0)}, \rho_\star) &= \frac{1}{4\pi\rho_\star^2} \sum_{i=1}^{n} \Bigg\{ \left[J_1\left(x_1^{(i)}, \frac{x_2^{(i)} + x_2^{(i+1)}}{2} \right) + \right. \\ &\quad \left. + J_1\left(x_1^{(i+1)}, \frac{x_2^{(i)} + x_2^{(i+1)}}{2} \right) \right] \left[x_2^{(i+1)} - x_2^{(i)} \right] - \\ &\quad - \left[J_2\left(\frac{x_1^{(i)} + x_1^{(i+1)}}{2}, x_2^{(i)} \right) + \right. \\ &\quad \left. + J_2\left(\frac{x_1^{(i)} + x_1^{(i+1)}}{2}, x_2^{(i+1)} \right) \right] \left[x_1^{(i+1)} - x_1^{(i)} \right] \Bigg\} \end{aligned} \quad (11)$$

where

$$\begin{aligned} J_1(x_1, x_2) &= \overline{I}^{-1} \int_0^{x_1} I[\boldsymbol{y}(x_1', x_2); \boldsymbol{y}^{(0)}, \rho_\star]\, \mathrm{d}x_1' , \\ J_2(x_1, x_2) &= \overline{I}^{-1} \int_0^{x_2} I[\boldsymbol{y}(x_1, x_2'); \boldsymbol{y}^{(0)}, \rho_\star]\, \mathrm{d}x_2' . \end{aligned} \quad (12)$$

and the brightness of the source, centered at $\boldsymbol{y}^{(0)}$ reads

$$I[\boldsymbol{y}(\boldsymbol{x});\boldsymbol{y}^{(0)},\rho_\star] = \overline{I}\times\begin{cases}\xi\left[\frac{|\boldsymbol{y}(\boldsymbol{x})-\boldsymbol{y}^{(0)}|}{\rho_\star}\right] \\ \qquad \text{for} \quad |\boldsymbol{y}(\boldsymbol{x})-\boldsymbol{y}^{(0)}|\leqslant\rho_\star \\ 0 \\ \qquad \text{for} \quad |\boldsymbol{y}(\boldsymbol{x})-\boldsymbol{y}^{(0)}|>\rho_\star\end{cases} \quad (13)$$

with $\overline{I}$ being the average surface brightness and $\xi(\rho)$ being the characteristic profile function depending on the fractional radius ρ.

However, $I[\boldsymbol{y}(\boldsymbol{x});\boldsymbol{y}^{(0)},\rho_\star]$ jumps at the source boundary $|\boldsymbol{y}(\boldsymbol{x})-\boldsymbol{y}^{(0)}|=\rho_\star$ if $\xi(1)\neq 0$, and its derivative at that position jumps if $(\mathrm{d}\xi/\mathrm{d}\rho)(1)\neq 0$. Similarly to the definition made by Dominik (1998) for a linear limb-darkening profile, this can be avoided for general monotically falling $\xi(\rho)$ by defining

$$\tilde{I}[\boldsymbol{y}(\boldsymbol{x});\boldsymbol{y}^{(0)},\rho_\star] = \overline{I}\times\begin{cases}\xi\left[\frac{|\boldsymbol{y}(\boldsymbol{x})-\boldsymbol{y}^{(0)}|}{\rho_\star}\right]+\xi(0)-2\xi(1) \\ \qquad \text{for} \quad |\boldsymbol{y}(\boldsymbol{x})-\boldsymbol{y}^{(0)}|\leqslant\rho_\star \\ \xi(0)-\xi\left[\frac{\rho_\star}{|\boldsymbol{y}(\boldsymbol{x})-\boldsymbol{y}^{(0)}|}\right] \\ \qquad \text{for} \quad |\boldsymbol{y}(\boldsymbol{x})-\boldsymbol{y}^{(0)}|>\rho_\star\end{cases}, \quad (14)$$

for which $\tilde{I}[\boldsymbol{y}(\boldsymbol{x});\boldsymbol{y}^{(0)},\rho_\star]\geqslant 0$. With the value of $I[\boldsymbol{y}(\boldsymbol{x})\boldsymbol{y}^{(0)},\rho_\star]$ for $|\boldsymbol{y}(\boldsymbol{x})-\boldsymbol{y}^{(0)}|>\rho_\star$ not affecting the integral, the magnification of the source can then be determined as

$$\begin{aligned} A(\boldsymbol{y}^{(0)},\rho_\star) &= \frac{1}{\pi\rho_\star^2}\int\frac{I[\boldsymbol{y}(\boldsymbol{x});\boldsymbol{y}^{(0)},\rho_\star]}{\overline{I}}\,\mathrm{d}x_1\,\mathrm{d}x_2 \\ &= \frac{1}{\pi\rho_\star^2}\Big\{\int\frac{\tilde{I}[\boldsymbol{y}(\boldsymbol{x});\boldsymbol{y}^{(0)},\rho_\star]}{\overline{I}}\,\mathrm{d}x_1\,\mathrm{d}x_2 \; - \\ &\qquad -[\xi(0)-2\xi(1)]\int\mathrm{d}x_1\,\mathrm{d}x_2\Big\}. \end{aligned} \quad (15)$$

5 CRITICAL CURVES OF BINARY LENSES

5.1 Topology

For studying the critical curves of a binary lens, it is favourable to center the coordinate system on the component with mass fraction m_1 rather than on the centre of mass as was done in Sect. 3.3, while keeping the line connecting the two components is along the y_1-axis. This means that for the two point lenses with mass fractions m_1 and $m_2=1-m_1$ that are separated by the angle $d\,\theta_\mathrm{E}$ one finds the lens equation

$$\boldsymbol{y}(\boldsymbol{x}) = \boldsymbol{x} - m_1\frac{\boldsymbol{x}}{|\boldsymbol{x}|^2} - (1-m_1)\frac{\boldsymbol{x}-(d,0)}{|\boldsymbol{x}-(d,0)|^2}\,, \quad (16)$$

where the coordinate system has been centered on the primary and the line connecting the two components is along the y_1-axis.

For every mass fraction m_1, the topology of the critical curves and the corresponding caustics undergo transitions at characteristic separations d_c and d_w, given by (Erdl & Schneider 1993)

$$\begin{aligned} m_1(1-m_1) &= \frac{1}{d_\mathrm{c}^8}\left(\frac{1-d_\mathrm{c}^4}{3}\right)^3, \\ d_\mathrm{w} &= \left[m_1^{1/3}+(1-m_1)^{1/3}\right]^{3/2}. \end{aligned} \quad (17)$$

This results in the three cases of close binaries ($d<d_\mathrm{c}$), intermediate binaries ($d_\mathrm{c}\leqslant d\leqslant d_\mathrm{w}$), and wide binaries ($d>d_\mathrm{w}$). For an equal-mass binary in particular, the transitions between the topologies occur at $d_\mathrm{c}=1/\sqrt{2}$ and $d_\mathrm{w}=2$ (Schneider & Weiß 1986). The three different topologies and their transitions are illustrated in Fig. 5, where the case $m_1=0.3$ has been used as example. For $d\to\infty$, the critical curves tend towards circles with radii $\sqrt{m_1}$ or $\sqrt{1-m_1}$ around each of the individual point mass, whereas the corresponding caustics are diamond-shaped with four cusps each, where two of these are on the y_1-axis, onto which the components of the lens binary fall, and tend towards points at the position of each point mass. As the two point masses approach, the inner cusps on the y_1-axis touch, as well as the corresponding critical points, so

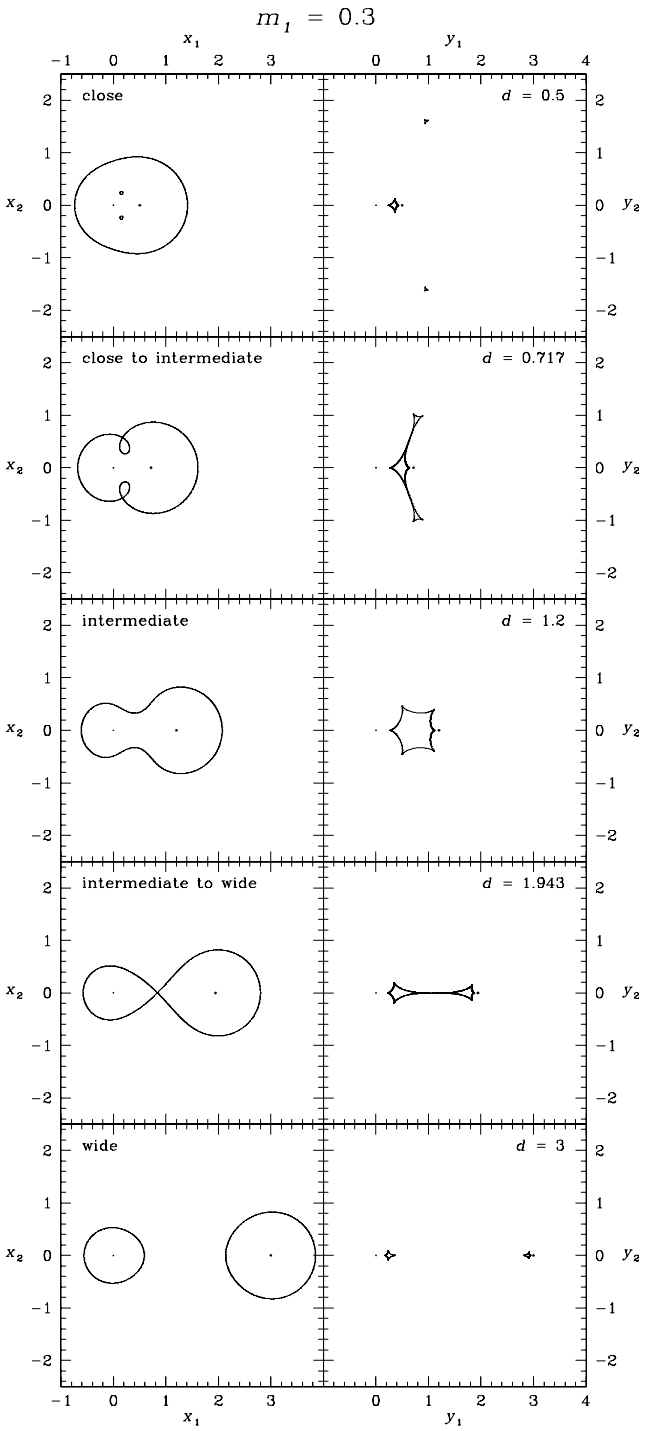

Figure 5. The three different topologies for the critical curves (left) and caustics (right) of binary point-mass lenses, illustrated for $m_1=0.3$, along with the transitions, which occur at separation parameters $d_\mathrm{c}=0.717$ or $d_\mathrm{w}=1.943$. The choice of the coordinate system corresponds to Eq. (16). Small dots indicate the positions of the two lens objects.

that the critical curve becomes a lying '8'. For intermediate binaries, i.e. $d_{\rm c} < d < d_{\rm w}$, there is a single closed critical curve in the shape of the bone, while the corresponding caustic contains 6 cusps, 2 of them being on the binary axis. Towards smaller separations, the fold line bends in and touches itself for $d = d_{\rm c}$, so that one outer and two inner closed curves result for a close binary, where $d < d_{\rm c}$. Correspondingly, the two upper or lower fold branches next to the on-axis cusps touch and the caustic detaches into a diamond-shaped 4-cusp caustic with two on-axis cusps and two triangular 3-cusp caustic with all those cusps being off-axis. As $d \to 0$, the outer critical curve tends to a circle of unit radius around the centre of mass, the inner critical curves contract towards a point and move towards the centre of mass. The outer critical curve corresponds to the diamond-shaped caustic, which tends towards a point at the centre of mass, whereas the triangular-shaped caustic, corresponding to the inner critical curves, decrease more strongly in size and move towards infinity.

5.2 Parametric representation

Using polar coordinates $\boldsymbol{x} = r(\cos\varphi, \sin\varphi)$, Erdl & Schneider (1993) have pointed out that critical points have to fulfill an equation of the form

$$a_2(r; d, m_1)\cos^2\varphi + a_1(r; d, m_1)\cos\varphi + a_0(r; d, m_1) = 0\,, \quad (18)$$

which can readily be solved for $\cos\varphi$ for any given r, so that critical curves can be parametrized by the radial coordinate r for each branch defined by the different values of $\cos\varphi$. In order to do so, however, one needs to find the ranges for r, for which critical points exist. The $\cos\varphi$-dependence gives two values $\varphi^{(+)} \in (0, \pi)$ or $\varphi^{(-)} \in (\pi, 2\pi)$, where $\varphi^{(+)} + \varphi^{(-)} = 2\pi$, for $-1 < \cos\varphi < 1$, which reflects the symmetry around the axis connecting the two lens components.

With

$$\begin{aligned} G &= r^2 + d^2\,, \\ H &= 2dr\,, \\ g &= 1 - \frac{m_1^2}{r^4}\,, \\ h &= \frac{2m_1(1-m_1)}{r^2}\,, \end{aligned} \quad (19)$$

Erdl & Schneider (1993) found

$$\begin{aligned} a_2(r; d, m_1) &= H^2 g - 2d^2 h\,, \\ a_1(r; d, m_1) &= H(h - 2Gg)\,, \\ a_0(r; d, m_1) &= G(Gg - h) + 2d^2 h - (1-m_1)^2\,. \end{aligned} \quad (20)$$

The existence of critical points requires the discriminant of the quadratic equation for $\cos\varphi$, Eq. (18), to be non-negative, i.e. $D \equiv a_1^2 - 4a_0a_2 \geqslant 0$ as well as $-1 \leqslant \cos\varphi \leqslant 1$. With Eq. (18), one finds the extreme values for $\cos\varphi$ to be assumed for $P_- \equiv a_2 - a_1 + a_0 = 0$ or $P_+ \equiv a_2 + a_1 + a_0 = 0$, respectively. This means that the number of solutions for $\cos\varphi$ can only change for $D = 0$, $P_- = 0$, or $P_+ = 0$, so that the respective values for r at given (d, m_1) define minimal or maximal values of branches (r, φ) of the critical curve. For $a_2 = 0$, i.e. $r = m_1^{1/4}$ irrespective of d, $C \equiv \cos\varphi$ has the unique solution $C = -a_0/a_1$ (for $a_2 = 0$ and $d > 0$, one always finds $a_1 \neq 0$) with Eq. (18), while one finds

$$C_\pm = -0.5[a_1 \pm (a_1^2 - 4a_0a_2)^{1/2}]/a_2\,, \quad (21)$$

where C_+ and C_- coincide for $D \equiv a_1^2 - 4a_0a_2 = 0$.

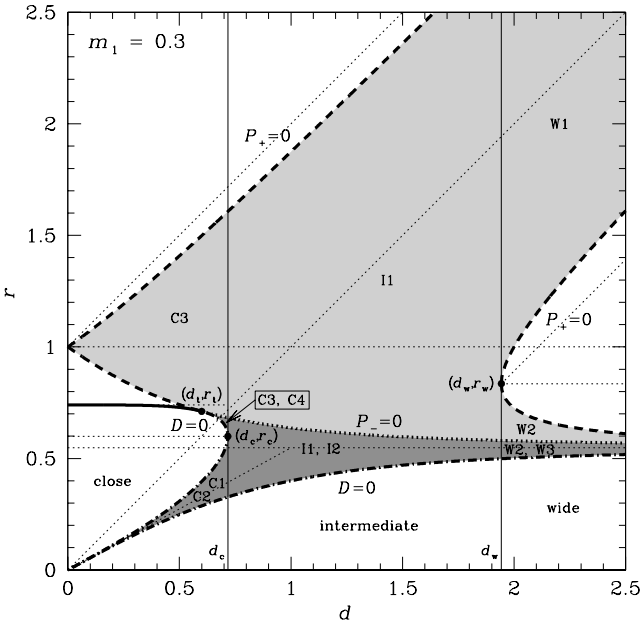

Figure 6. Structure of the branches of the critical curve (r, φ) indicated by the allowed ranges $[r_{\rm min}, r_{\rm max}]$ for r marked by thick lines, which correspond to $D = 0$, $P_- = 0$, or $P_+ = 0$. The line type reflects the matching value of $\cos\varphi$, either C_+ or C_-, Eq. (21). While dashed lines indicate a limit for r with C_+, dotted lines refer to a limit with C_-, and dash-dotted lines with both. The solid part of the $D = 0$ contour refers to neither. Bracket intervals for the critical radii, as listed in Table 1, are indicated by thin dotted lines. The lighter shaded region marks the range for which a solution with C_+ exists, whereas the darked shades region marks the range for which both solutions with either C_+ or C_- exist. The classification of the branches as C1 to C4, I1 and I2, and W1 to W3 for close, intermediate or wide binaries, is shown in Table 2. The transitions between the topologies are indicated by thin solid lines while the points where the critical curves touch are marked as $(d_{\rm c}, r_{\rm c})$ or $(d_{\rm w}, r_{\rm w})$. The contours for $D = 0$ and $P_- = 0$ touch at $(d_{\rm t}, r_{\rm t})$.

Fig. 6 shows the allowed ranges for r as a function of d using $m_1 = 0.3$ as example. However, the structure of the solutions does not depend on the adopted mass fraction. While for given (d, m_1), there is at least one and up to three solutions for $D = 0$, denoted in the following by $r_D^{(1)}, r_D^{(2)}, r_D^{(3)}$, and $P_+ = 0$, denoted by $r_{P_+}^{(1)}, r_{P_+}^{(2)}$, and $r_{P_+}^{(3)}$, there is always just a single solution for $P_- = 0$, denoted by r_{P_-}. The two additional solutions for $D = 0$ are only present for close binaries, whereas the two additional solutions for $P_+ = 0$ exist for wide binaries. These critical radii can be obtained by interval bisection using the initial bracket intervals listed in Table 1, which are also indicated by small dotted lines in Fig. 6. For $d = 0$, one finds $r_{P_-} = r_{P_+}^{(1)} = 1$ which reflects the outer critical curve tendings towards the constant $r = 1$ (Einstein circle), while $r_D^{(1)} = r_D^{(2)} = 0$ reflects the inner critical curves contracting at the origin. Moreover, $r_D^{(3)} = m_1^{1/4}$ for $d = 0$, but this is not a valid value, because $\cos\varphi$ is out of the allowed range.

Table 2 lists the branches of the critical curve defined by the allowed range $[r_{\rm min}, r_{\rm max}]$ for r and the value for $\cos\varphi$, either C_+ or C_- as defined by Eq. (21). While C1 and C2 correspond to the small two inner critical curves, C3 and C4 represent the outer critical curve. Branch C4 only exists for $d_{\rm t} < d < d_{\rm c}$, where $d_{\rm t}$ is the separation for which the curves $D = 0$ and $P_- = 0$ touch. These conditions imply $a_2 = a_0$, so that $a_1 = 2a_0$ or $a_1 = 2a_2$. For

Table 1. Bracket intervals for the critical radii defining the branches of the critical curves of a binary point-mass lens.

Critical radius	Bracket interval	Separation
r_{P_-}	$(m_1^{1/2}, 1]$	
$r_{P_+}^{(1)}$	$(d, d+1)$	
$r_{P_+}^{(2)}$	$[d-d_\mathrm{w}+r_\mathrm{w}, d)$	$d > d_\mathrm{w}$
$r_{P_+}^{(3)}$	$(m_1^{1/2}, r_\mathrm{w}]$	$d > d_\mathrm{w}$
$r_D^{(1)}$	$(0, \min\{m_1^{1/2}d, m_1^{1/2}\})$	
$r_D^{(2)}$	$(m_1^{1/2}d, r_\mathrm{c}]$	$d < d_\mathrm{c}$
$r_D^{(3)}$	$[r_\mathrm{c}, m_1^{1/4}]$	$d < d_\mathrm{c}$

For given mass fraction m_1 and separation parameter d, critical radii need to fulfill $P_- = 0$, $P_+ = 0$, or $D = 0$. These roots can be found by interval bisection of the respective bracket interval. $r_D^{(1)}$ and $r_D^{(2)}$ are separated by the asymptotic solution $m_1^{1/2}d$ for $d \to 0$.

Table 2. Branches of the critical curves defined by the range of the radial coordinate r and the branch of $\cos\varphi$, defined by Eq. (21).

Branch	Range of r	$\cos\varphi$	Separation
C1	$[r_D^{(1)}, r_D^{(2)}]$	C_+	$d < d_\mathrm{c}$
C2	$[r_D^{(1)}, r_D^{(2)}]$	C_-	$d < d_\mathrm{c}$
C3	$[r_{P_-}, r_{P_+}^{(1)}]$	C_+	$d \leqslant d_\mathrm{t} < d_\mathrm{c}$
C3	$[r_D^{(3)}, r_{P_+}^{(1)}]$	C_+	$d_\mathrm{t} < d < d_\mathrm{c}$
C4	$[r_D^{(3)}, r_{P_-}]$	C_-	$d_\mathrm{t} < d < d_\mathrm{c}$
I1	$[r_D^{(1)}, r_{P_+}^{1}]$	C_+	$d_\mathrm{c} \leqslant d \leqslant d_\mathrm{w}$
I2	$[r_D^{(1)}, r_{P_-}]$	C_-	$d_\mathrm{c} \leqslant d \leqslant d_\mathrm{w}$
W1	$[[r_{P_+}^{(2)}, r_{P_+}^{(1)}]$	C_+	$d > d_\mathrm{w}$
W2	$[r_D^{(1)}, r_{P_+}^{(3)}]$	C_+	$d > d_\mathrm{w}$
W3	$[r_D^{(1)}, r_{P_-}]$	C_-	$d > d_\mathrm{w}$

Branches C1–C4 refer to the close-binary case, I1/I2 to the intermediate binary and W1–W3 to wide binaries, where transitions occur at d_c and d_w, which depend on m_1. At d_t, the curves $D = 0$ and $P_- = 0$ touch, so that branch C4 only exists for $d_\mathrm{t} < d < d_\mathrm{c}$.

$d \to 0$, C3 tends to the Einstein circle, whereas C1 and C2 degenerate into points. For $d = d_\mathrm{c}$, the inner critical curves touch the outer one at the radius $r_\mathrm{c} = (m_1 d_\mathrm{c})^{1/3}$, where C1 and C3 merge into I1, and C2 and C4 merge into I2. For the intermediate binary, I2 is the branch near the object with mass fraction m_1 at the coordinate origin, whereas I1 is the far branch. For wide binaries, W1 gives the critical curve around the far object, while W2/W3 surround the near object, which both tend to circles around the respective object. At $d = d_\mathrm{w}$, the critical curves described by branches W1 and W2 merge at radius $r_\mathrm{w} = (m_1 d_\mathrm{w})^{1/3}$ into I2, whereas W3 and I2 are identical.

5.3 Cusps and fold lines

In order for the determinant of the Jacobian $(\partial\boldsymbol{y}/\partial\boldsymbol{x})$ of the lens mapping to vanish, at least one of its eigenvalues must be zero. In two dimensions, singularities for which there are no non-zero eigenvalues cannot be a generic feature. In fact, such singularities (known as umbilics) do not exist for any binary point-mass lens (Schneider & Weiß 1986; Erdl & Schneider 1993). Therefore, we can restrict ourselves to the case of exactly one eigenvalue being zero for dicussing the critical curves of binary lenses.

Since the critical curve is defined as the set of points where the Jacobian determinant of the lens mapping vanishes, Eq. (4), the unit normal vector is given as $\boldsymbol{n} = \boldsymbol{D}/|\boldsymbol{D}|$, where $\boldsymbol{D} = \nabla \det\left(\frac{\partial \boldsymbol{y}}{\partial \boldsymbol{x}}\right)$. A corresponding tangent vector then follows as $\boldsymbol{t}_{\boldsymbol{x}} = (-n_2, n_1)$, and $\boldsymbol{t}_{\boldsymbol{y}} = \left(\frac{\partial \boldsymbol{y}}{\partial \boldsymbol{x}}\right)\boldsymbol{t}_{\boldsymbol{x}}$ is a tangent to the caustic. Therefore, the caustic is a smooth curve with defined tangent direction (fold singularity) as long as $\boldsymbol{t}_{\boldsymbol{x}}$ is not an eigenvector $\boldsymbol{e}_0$ of the Jacobian to the eigenvalue zero (cusp singularity). A cusp is therefore defined by the scalar equation $\boldsymbol{n} \cdot \boldsymbol{e}_0 = 0$.

In order to identify cusps as roots of $\boldsymbol{n} \cdot \boldsymbol{e}_0$, one needs to find $\boldsymbol{e}_0$ as a smooth function along the critical curve. However, based on just the local Jacobian

$$\left(\frac{\partial \boldsymbol{y}}{\partial \boldsymbol{x}}\right) = \begin{pmatrix} y_{11} & y_{12} \\ y_{12} & y_{22} \end{pmatrix}, \tag{22}$$

where $y_{ij} = \partial x_i/\partial x_j$ and $y_{ij} = y_{ji}$, there is no such global solution. With $y_{11}y_{22} - y_{12}^2 = 0$, one finds that

$$y_{11} = 0 \vee y_{22} = 0 \Leftrightarrow y_{12} = 0\,, \tag{23}$$

i.e. the Jacobian is diagonal if and only if one of the diagonal elements is zero, which reflects the requirement that one eigenvalue has to be zero. Moreover $y_{11} + y_{22} = 2$, i.e. the trace of the Jacobian is 2 and the non-zero eigenvalue is 2. Since the condition for a critical point implies that $y_{11}y_{22} \geqslant 0$, one finds $-1 \leqslant y_{12} \leqslant 1$, $0 \leqslant y_{11} \leqslant 2$, and $0 \leqslant y_{22} \leqslant 2$. As long as $y_{11} \neq 0$, an eigenvector to the eigenvalue zero is given by $\boldsymbol{e}_0^{(1)} = (-y_{12}, y_{11})$, but it flips over as y_{11} passes through zero, since y_{12} changes sign at that instance. Similarly, $\boldsymbol{e}_0^{(2)} = (y_{22}, -y_{12})$ is an eigenvector to the eigenvalue zero for $y_{22} \neq 0$, which flips over as y_{22} passes through zero. This means that the branches of the critical curves or caustics need further subdivision.

However, the relative positions of the cusps, the points where the Jacobian is diagonal and the points where the branches of $\cos\varphi$ merge, are unique characteristics for each topology, as shown in Fig. 7. Without restriction of generality, one can assume $m_1 \leqslant 0.5$ (otherwise simply mirror the coordinates with respect to the vertical axis). From this figure, one can read off how to determine the positions of the cusps as well as those points for which $y_{11} = 0$ or $y_{22} = 0$ by sucessive bracketing using an interval bisection algorithm for root finding.

Choosing $\boldsymbol{e}_0^{(2)}$ as the adaptation of $\boldsymbol{e}_0$ for all λ where $y_{22} \neq 0$, minimized the required number of subbranches, since several positions with $y_{22} = 0$ coincide with the points where the critical curve crosses the x_1-axis or the respective caustic crosses the y_1-axis.

5.4 Finding caustic-associated images

If the source includes a cusp, there is no image area that is disconnected from the image position(s) of the source centre. That case can only arise if the source contour crosses a contiguous fold line between cusps twice. Since the caustic $\boldsymbol{y}_\mathrm{c}(\lambda)$ is a smooth function of the parameter λ between cusps, a circular contour centered around $\boldsymbol{y}^{(0)}$ can only cross it twice if the distance

$$d(\lambda; \boldsymbol{y}^{(0)}) \equiv \left[\boldsymbol{y}_\mathrm{c}(\lambda) - \boldsymbol{y}^{(0)}\right]^2 \tag{24}$$

exhibits a local minimum, so that

$$\frac{\mathrm{d}d(\lambda; \boldsymbol{y}^{(0)})}{\mathrm{d}\lambda} = \frac{\mathrm{d}\boldsymbol{y}_\mathrm{c}(\lambda)}{\mathrm{d}\lambda} \cdot \left[\boldsymbol{y}_\mathrm{c}(\lambda) - \boldsymbol{y}^{(0)}\right] = 0 \tag{25}$$

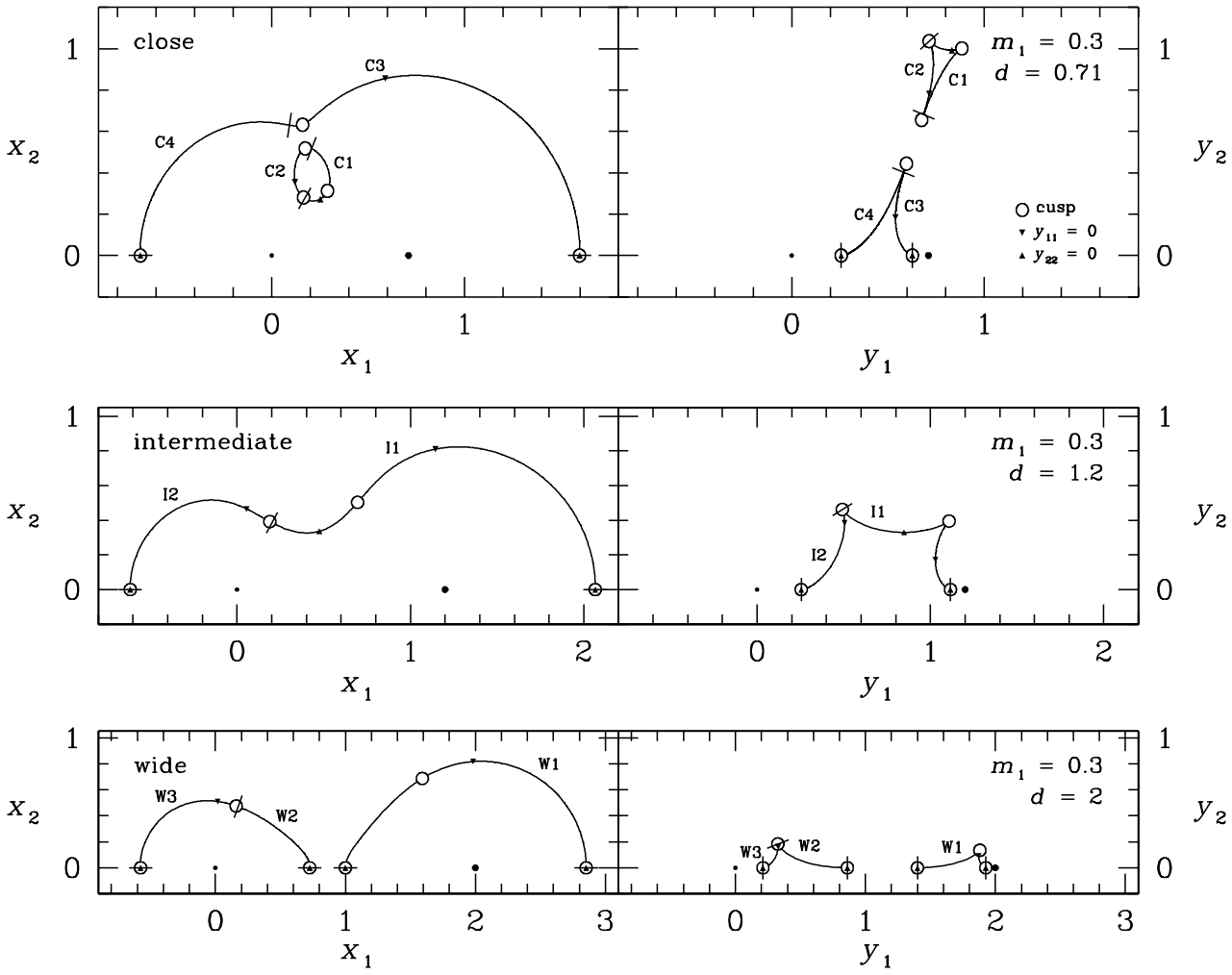

Figure 7. Branches of the critical curves and caustics for the three different topologies (wide, intermediate, close). Perpendicular lines separate the different ranges for r and $\cos\varphi$ as listed in Table 2, whereas triangles mark the points for which the Jacobian becomes diagonal, i.e. either $y_{11} = 0$ (pointing downward) or $y_{22} = 0$ (pointing upward), and cusps are indicated by circles. Filled dots mark the position of the two point masses, where the respective areas are proportional to the fractional mass. The nomenclature of the branches corresponds to Table 2. For $d \leqslant d_\mathrm{t}$, branch C4 vanishes, while C3 extends between both intersections of the critical curve with the x_1-axis or both intersections of the caustic with the y_1-axis, respectively.

constitutes a necessary condition, which means that the tangent to the caustic has to be perpendicular to the line connecting it with the source centre. Only such points can therefore constitute the remaining image positions that need to be inserted into the adaptive grid in order to ensure that all image contours are found.

If the parameter λ is chosen as length of the critical curve, one finds

$$\frac{\mathrm{d}}{\mathrm{d}\lambda} = n_1 \frac{\partial}{\partial x_2} - n_2 \frac{\partial}{\partial x_1}\,, \tag{26}$$

with $\boldsymbol{n}$ being is the unit normal vector.

If the curvature $\kappa_{\boldsymbol{y}}(\lambda)$ of the caustic is a monotonic function over the considered range $[\lambda_\mathrm{min}, \lambda_\mathrm{max}]$, the distance $d(\lambda; \boldsymbol{y}^{(0)})$ can only have a single extremum. Therefore, for each caustic segment, a potential root of $\mathrm{d}\kappa_{\boldsymbol{y}}/\mathrm{d}\lambda$ is determined, providing the final subdivision. With $\boldsymbol{t}_{\boldsymbol{y}}(\lambda)$ denoting the caustic tangent, the curvature is given as

$$\kappa_{\boldsymbol{y}}(\lambda) = \frac{t_{\boldsymbol{y},1} t'_{\boldsymbol{y},2} - t'_{\boldsymbol{y},1} t_{\boldsymbol{y},2}}{|\boldsymbol{t}_{\boldsymbol{y}}|^3}\,, \tag{27}$$

where the prime denotes the derivative with respect to λ, as defined by Eq. (26). By further differentiation with respect to λ, $\mathrm{d}\kappa_{\boldsymbol{y}}/\mathrm{d}\lambda$ arises as analytical function of up to the 4th derivatives of $\boldsymbol{y}(\boldsymbol{x})$ with respect to x_1 or x_2.

6 APPLICATIONS AND LIMITATIONS

Fig. 8 shows example light curves for circular sources with different radii and different brightness profiles affected by a binary gravitational lens, characterized by the separation parameter $d = 1.2$ and the mass fraction $m_1 = 0.3$. For the smaller source radii ($\rho_\star = 0.05$ and $\rho_\star = 0.1$), the source transits the caustic and moves completely inside, so that separated fold-caustic passages produce distinct characteristic peaks that can be described by a generic profile function (e.g. Dominik 2004). In these cases, the insertion of a seed image mapping to a local minimum of the distance of the source centre from the caustic was essential. In contrast, the source never moves completely inside the caustic for $\rho_\star = 0.2$ or $\rho_\star = 0.5$. For $\rho_\star = 0.2$, there are epochs for which the source

crosses the same fold line (as for the smaller radii) or different adjoining fold lines, with or without the cusp in between. Moreover, for $\rho_\star = 0.5$ there are epochs for which a various number of up to three cusps are enclosed by the source.

For $\rho_\star = 0.5$, a light curve for a brightness profile corresponding to maximal limb darkening, i.e.

$$\xi(\rho) = \frac{3}{2}\sqrt{1-\rho^2}\,, \tag{28}$$

is shown along with that for a uniformly bright source. With a smaller fraction of the total brightness in the outer parts for the limb-darkened source, the source magnification shows a smaller rise as the source enters or exits the caustic but is larger in between.

The application of Green's theorem to replace the integration over the image area by an integration along its boundary is a very efficient approach if the images are moderately distorted, so that a large area for the given boundary length is enclosed (a circle is optimal). There is significantly less gain, however, for extremely strong distortions leading to the enclosed area resembling a line. This case is indeed approached if a source star gets very closely aligned with a lens star that is only associated with much less massive companions such as orbiting planets. Resulting in large peak magnifications, such configurations are of some specific interest due to their planet-detection potential (Griest & Safizadeh 1998; Rattenbury et al. 2002). For modelling the event with the largest peak magnification recorded so far, OGLE 2004-BLG-343 with $A_0 \sim 3000$, Dong et al. (2006) have derived a more efficient variant of the ray-shooting technique. In fact, the current version of the adaptive contouring algorithm is significantly slowed down for very small impact angles between source and planet-surrounded lens star, but, for uniformly bright sources, the computation of a single magnification with a relative uncertainty of 5×10^{-4} can still be carried out in ~ 200 ms on a 600 MFlops machine for magnifications in the range $A \sim 100$–1000, while a result is obtained about 20 times faster (~ 10 ms) for moderate $A \sim 3$. It turns out that the same choice for the accuracy parameter ε (Sect. 4) provides a more accurate result for larger magnifications. For limb-darkened sources, one needs to add another numerical integration, which slows down the computation a lot. Determining the magnification of limb-darkened sources by integrating along the image boundary therefore becomes inefficient for highly-distorted images. In this case, alternative techniques should be used. However, the adaptive grid approach can be combined with other evaluations of the image area or magnification. Moreover, limb darkening usually adds a small shift to the magnification, so that all other parameters can be well approximated by assuming a uniformly bright source during an initial search (allowing faster computation), whereas limb darkening only needs to be taken into account in a final refinement step. For source stars idealized to be uniformly bright, the adaptive contouring algorithm appears to be much faster than ray-shooting for moderate magnifications, while providing a smaller gain for huge magnifications, which however can still be substantial (~ 4) for $A \sim 100$. Since the computation of ray-shooting magnification maps for a fixed $(d, q, \rho_\star)$ takes at least some minutes, the evaluation of a several hundred data points by adaptive contouring usually appears to be faster.

7 SUMMARY AND CONCLUSIONS

The presented adaptive contouring algorithm provides an efficient way for calculating microlensing light curves, i.e. the combined magnification of the images as a function of time. While the use of an adaptive grid prevents wasting time by densely covering regions of little interest, it can be ensured that for binary lenses no image is missed. This is achieved by finding the images of the source centre by solving a fifth-order complex polynomial (Witt & Mao 1995), realizing that holes in the images must include the position of one of the lens components, and by identifying a position inside images stretching over a critical curve making use of its parametrization found by Erdl & Schneider (1993).

The efficiency of the proposed algorithm can be enhanced by using a prioritization scheme for the subdivision of squares containing the image contour line (double-adaptive contouring) rather than using a common resolution depth, by using a better estimate on the uncertainty of the calculated magnification, or using a better approximation of the contour line and its enclosed area or the source magnification.

While the performance of the current implementation is impressive for weakly-distorted images, the computation gets significantly slowed down if images are strongly distorted, i.e. nearly degenerate into lines. For limb-darkened sources, the evaluation of the magnification by an integration along a contour line becomes inefficient for such images. However, the adaptive grid approach could be combined with other evaluation algorithms.

As already pointed out by Dominik (1998), the presented approach can also be used for calculating the astrometric microlensing signal, i.e. the positional variation of the centroid of light composed of the images.

The identification of cusps and the parametrization of the branches of the critical curve in between can also serve as basis for algorithms searching for matching binary-lens parameters of microlensing features where the source passes over a fold- or cusp caustic.

An implementation in C is available from the author and can be downloaded from `http://star-www.st-and.ac.uk/~md35/Software.html`.

ACKNOWLEDGMENTS

I would like to thank Keith Horne for reading and commenting on the manuscript, and acknowledge support by PPARC rolling grant PPA/G/O/2001/00475. Special thanks go to Subo Dong for running some tests with his modified ray-shooting code that allowed a comparison of efficiency.

REFERENCES

Dominik M., 1995, A&AS, 109, 597
Dominik M., 1998, A&A, 333, L79
Dominik M., 2004, MNRAS, 353, 69
Dong S., et al., 2006, ApJ, 642, 842
Einstein A., 1936, Science, 84, 506
Erdl H., Schneider P., 1993, A&A, 268, 453
Gould A., 1994, ApJ, 421, L71
Griest K., Safizadeh N., 1998, ApJ, 500, 37
Kayser R., Refsdal S., Stabell R., 1986, A&A, 166, 36
Rattenbury N. J., Bond I. A., Skuljan J., Yock P. C. M., 2002, MNRAS, 335, 159
Schneider P., Weiß A., 1986, A&A, 164, 237
Schneider P., Weiß A., 1987, A&A, 171, 49
Schneider P., 1985, A&A, 143, 413
Schramm T., Kayser R., 1987, A&A, 174, 361

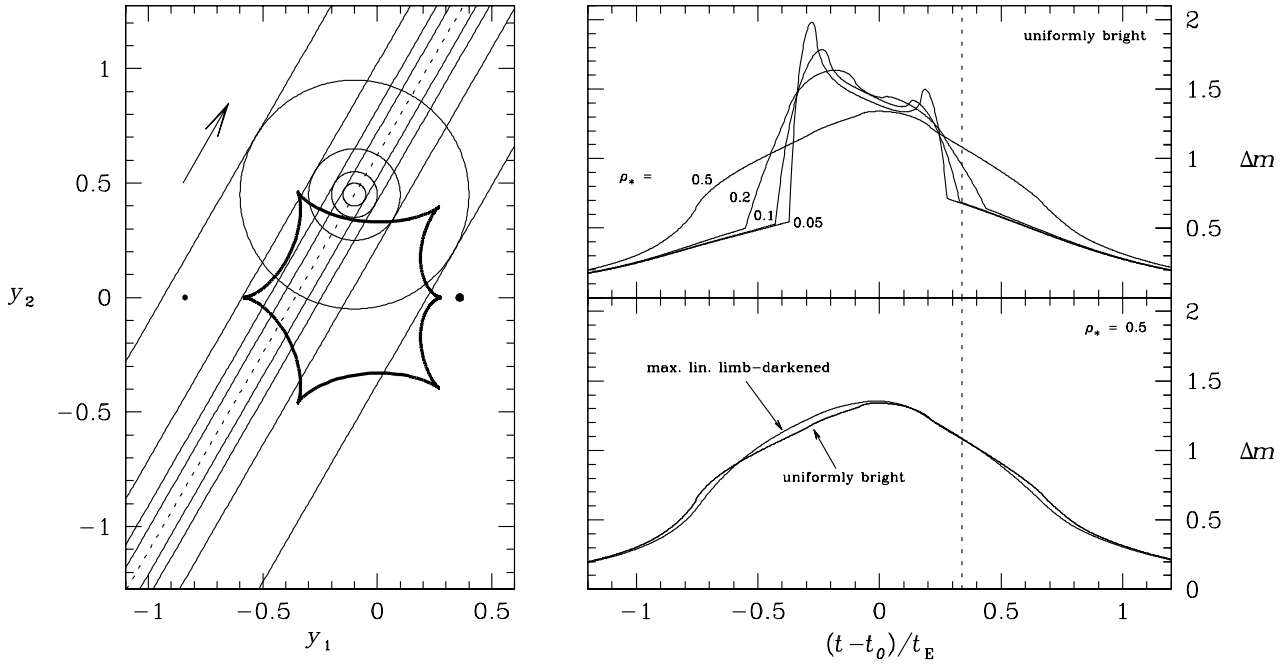

Figure 8. Example light curves for sources of different radii and with different brightness profiles affected by a binary lens. The components of the lens binary have mass fractions $m_1 = 0.3$ (left) and $1 - m_1 = 0.7$ (right) and their separation in units of the angular Einstein radius $\theta_{\rm E}$ is given by $d = 1.2$. The source is assumed to move uniformly with respect to the lens at an angle of 60° with respect to the binary-lens axis and to pass through $\boldsymbol{y}^{(0)} = (-0.1, 0.45)$, where the coordinates $\boldsymbol{y}$ refer to the angular source position in units of the angular Einstein radius $\theta_{\rm E}$ with respect to the centre of mass of the lens system. The arrow shows the direction of motion, where the source moves by the angle $\theta_{\rm E}$ within the time $t_{\rm E}$. Circles show the snapshot of the source for different radii as it passes through $\boldsymbol{y}^{(0)} = (-0.1, 0.45)$, while straight lines limit the region of the plane traced by it and a dotted line shows the trajectory of the source centre. A thick line shows the caustic, while the positions of the components of the binary lens are indicated by dots whose sizes reflect the mass fractions. The epoch t_0 refers to the closest approach of the source to the centre of mass of the lens binary, whereas the time at which the source reaches $\boldsymbol{y}^{(0)} = (-0.1, 0.45)$ is indicated by a vertical dashed line in the plots showing the light curves. The magnification is shown as decrease in magnitude $\Delta m = 2.5 \log A$.

Witt H. J., Mao S., 1994, ApJ, 430, 505
Witt H. J., Mao S., 1995, ApJ, 447, L105